Winter January 13, 2015

Nanocrystals for Luminescent Solar Concentrators

Stephen R. McDowall, *Western Washington University*
Liam R Bradshaw, *Western Washington University*
Kathryn E Knowles, *University of Washington*
Daniel R. Gamelin, *University of Washington*

NANO LETTERS

Letter

pubs.acs.org/NanoLett

Nanocrystals for Luminescent Solar Concentrators

Liam R. Bradshaw,[†] Kathryn E. Knowles,[†] Stephen McDowall,[‡] and Daniel R. Gamelin*,[†]

[†]Department of Chemistry, University of Washington, Seattle, Washington 98195-1700, United States

[‡]Mathematics Department, Western Washington University, 516 High Street, Bellingham, Washington 98225, United States

Supporting Information

ABSTRACT: Luminescent solar concentrators (LSCs) harvest sunlight over large areas and concentrate this energy onto photovoltaics or for other uses by transporting photons through macroscopic waveguides. Although attractive for lowering solar energy costs, LSCs remain severely limited by luminophore reabsorption losses. Here, we report a quantitative comparison of four types of nanocrystal (NC) phosphors recently proposed to minimize reabsorption in large-scale LSCs: two nanocrystal heterostructures and two doped nanocrystals. Experimental and numerical analyses both show that even the small core absorption of the leading NC heterostructures causes major reabsorption losses at relatively short transport lengths. Doped NCs outperform the heterostructures substantially in this critical property. A new LSC phosphor is introduced, nanocrystalline $Cd_{1-x}Cu_xSe$, that outperforms all other leading NCs by a significant margin in both small- and large-scale LSCs under full-spectrum conditions.

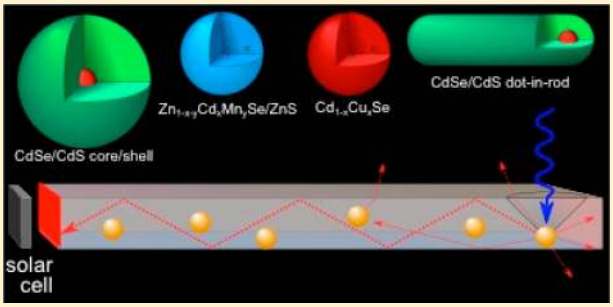

KEYWORDS: *Luminescent solar concentrator, phosphor, doped nanocrystal, nanocrystal heterostructure*

Luminescent solar concentrators (LSCs) are antenna systems that harvest sunlight and concentrate photons through the processes of photon absorption, luminescence, and waveguiding. One attractive LSC device comprises a planar waveguide containing embedded luminophores with photovoltaics (PVs) mounted at the waveguide edges, as depicted in Figure 1A. In this device, the concentrated photons are converted to electricity by the PVs, allowing large-area solar harvesting while requiring only small-area PVs. Such LSCs can possibly lower the cost of solar energy.[1−3] Specific LSC applications include solar collectors for integration into smart windows, electronic devices, or fiber optics,[3,4] photon transport for passive daylighting,[5,6] and active color filters (e.g., in tandem PV cells[7] or greenhouse panels[8]). Regardless of their specific application, LSCs universally rely on photon transport over macroscopic distances, which makes them susceptible to a variety of loss mechanisms. For a waveguide as in Figure 1A made of glass or plastic ($n \sim 1.5$), approximately 75% of the emitted photons are successfully trapped in waveguide modes[1] with the remainder lost to the "escape cone" defined by Snell's law. Photons that are captured by total internal reflection can still be lost via scattering from the waveguide surface, internal defects, or even the luminophores themselves (such as with microcrystalline phosphors[9]), or via reabsorption by the luminophores followed by nonradiative decay or emission into the escape cone. Reabsorption losses have historically limited practical implementation of large-scale LSCs.[3,10,11]

Recent advances in the synthesis of luminescent nanocrystals (NCs) with high photoluminescence (PL) quantum yields, tunable solar absorption, and good photostability have stimulated interest in nanocrystals for LSC technologies.[12−14] Several reports have proposed that NCs can solve the reabsorption problem.[15−19] One strategy for eliminating self-absorption involves the growth of NC heterostructures that integrate wider-gap semiconductors with small cores having a narrower bandgap (e.g., CdS on CdSe cores, Figure 1B-i,ii).[15,18,19] In such NCs, the wider-gap material dominates the absorption spectrum, and red-shifted luminescence occurs either from the core or from spatially indirect transitions across the heterointerface. Large shell/core volume ratios imply small relative absorption from the luminescent excited state. Doped semiconductor NCs have also been demonstrated to show small LSC reabsorption losses.[17] In Mn^{2+}-doped ZnSe NCs, for example, the NC efficiently sensitizes excitation of Mn^{2+} impurity ions to their $^4T_1$ ligand-field excited state, which emits with high quantum yield and a very large effective Stokes shift that results in little or no reabsorption losses in the corresponding LSCs.[17]

The vastly different device configurations used in previous studies of nanocrystal LSCs make direct comparison of nanocrystal performance difficult. For example, device thicknesses ranged from a few hundred microns[16,17] to over 1 cm,[15,18] and transverse optical densities at the NCs' first absorption features (OD_t) ranged from 0.1 to 0.6. Both of these parameters affect reabsorption, which is proportional to the concentration of luminophore and hence determined by the ratio of OD_t to waveguide thickness (t) according to Beer's law.

Received: November 25, 2014
Revised: January 3, 2015
Published: January 13, 2015

DOI: 10.1021/nl504510t
Nano Lett. 2015, 15, 1315−1323

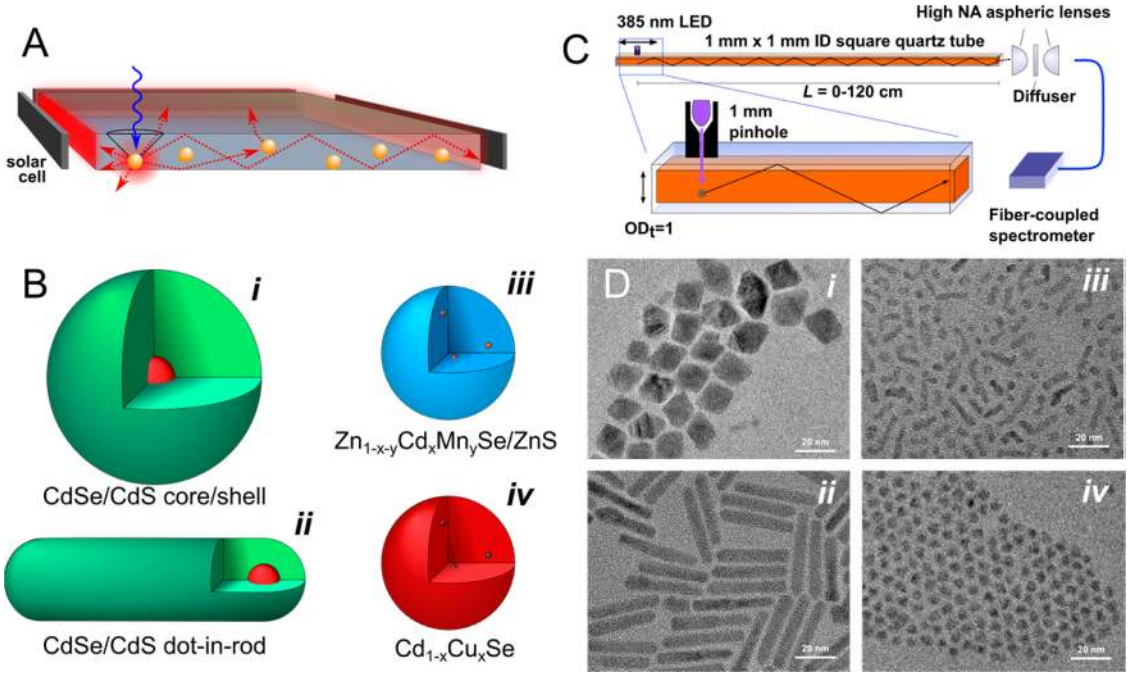

Figure 1. (A) A typical planar LSC configuration in which a luminophore (yellow spheres) is incorporated into a waveguide material surrounded on all edges by solar cells. Sunlight (blue arrow) is absorbed by the luminophore, and the luminescence (red arrows) is waveguided to the solar cells at the edges. (B) Schematic depictions of four types of nanocrystals proposed for use in LSCs. (C) Schematic depiction of the apparatus used for measuring excitation distance dependent PL spectra. (D) TEM images of the NCs investigated here: (i) CdSe/CdS core/shell NCs, (ii) CdSe/CdS dot-in-rod NCs, (iii) $Zn_{0.87}Cd_{0.11}Mn_{0.02}Se/ZnS$ NCs, and (iv) representative $Cd_{0.999}Cu_{0.001}Se$ NCs.

For practical applications, both OD_t and t will undoubtedly require careful optimization in planar 2D LSCs based on physical and economic criteria, and developments in microcell LSCs[20,21] or other configurations may even lead to entirely new structural paradigms. In parallel, the physical properties of NCs can be optimized independently to yield a portfolio of luminophores that will excel in many different LSC device configurations.

Here, we report the quantitative assessment of four types of nanocrystals as potential LSC luminophores: the CdSe/CdS core/shell and dot-in-rod heterostructures of Figure 1B-i,ii, and two new doped-nanocrystal LSC phosphors. In one, we have modified our previously reported motif of Mn^{2+}-doped ZnSe NCs by incorporating Cd^{2+} to increase solar absorption (Figure 1B-iii). For capture of an even broader portion of the solar spectrum, we have also used narrower-gap CdSe NCs to sensitize Cu^{+} luminescence (Figure 1B-iv). To date, there have been no reports of any copper-doped NC LSCs or of Mn^{2+}-doped $Zn_{1-x}Cd_xSe$ NC LSCs. The synthetic techniques used to make both of these types of doped NCs described here yield the highest PL quantum yields reported to date for these materials.

Using a one-dimensional liquid waveguide with translatable excitation (Figure 1C) as a standard device geometry, we have quantified the reabsorption losses of these four types of nanocrystals by measuring their luminescence spectra as a function of photon transport distance, L, up to 1.2 m, encompassing the length scales considered relevant for practical solar windows, panels, or daylighting, for example. These measurements agree well with the reabsorption probabilities predicted from NC absorption and PL spectra. The results show that reabsorption losses remain a major problem for the two leading heterostructured NC phosphors but are more effectively eliminated in both types of doped semiconductor NCs. In particular, the copper-doped NCs are found to be the "best-in-class" phosphors for full-spectrum applications, outperforming the other nanocrystals in total solar concentration at both short and long LSC lengths. In addition to highlighting doped NCs as a promising new class of LSC luminophores, this work provides a benchmark for quantitative evaluation of new LSC luminophores developed in the future.

Nanocrystals of the types illustrated in Figure 1B were prepared by literature methods (see Experimental Methods). Figure 1D shows representative TEM images of the CdSe/CdS core/shell NCs, CdSe/CdS dot-in-rod NCs, $Zn_{0.87}Cd_{0.11}Mn_{0.02}Se/ZnS$ NCs, and $Cd_{0.999}Cu_{0.001}Se$ NCs used in this study. The core/shell NCs of Figure 1D-i and the dot-in-rod NCs of Figure 1D-ii were grown using the same d = 2.7 nm wurtzite CdSe cores. The CdSe/CdS core/shell NCs appear to be octahedrally faceted with an average side length of 13.5 nm, implying a CdS/CdSe volume ratio of 114:1. The CdSe/CdS dot-in-rod NCs have an average overall dimension of 6.1 nm × 32.2 nm, and a CdS/CdSe volume ratio of 110:1. Figure 1D-iii shows $Zn_{0.87}Cd_{0.11}Mn_{0.02}Se/ZnS$ NCs with an average diameter of 3.8 nm, some of which appear to have undergone "oriented attachment"[22] to form short rods.[23] The $Zn_{0.87}Cd_{0.11}Mn_{0.02}Se$ cores showed an average diameter of 3.2 nm and a similar distribution of shapes. The $Cd_{0.999}Cu_{0.001}Se$ NCs shown in Figure 1D-iv appear roughly spherical with an average diameter of 5.7 nm.

Figure 2A plots absorption and PL spectra of solutions of the same NCs, all with concentrations adjusted to reach OD ~ 1 at the first intense absorption feature in a 1 mm path length cuvette. The wavelengths of these first absorption features (λ_{thresh}) are listed in Table 1. These data confirm previously reported spectra of similar samples. From these spectra, all samples appear to have minimal overlap between absorption and luminescence, as desired for LSC applications. It is

DOI: 10.1021/nl504510t
Nano Lett. 2015, 15, 1315−1323

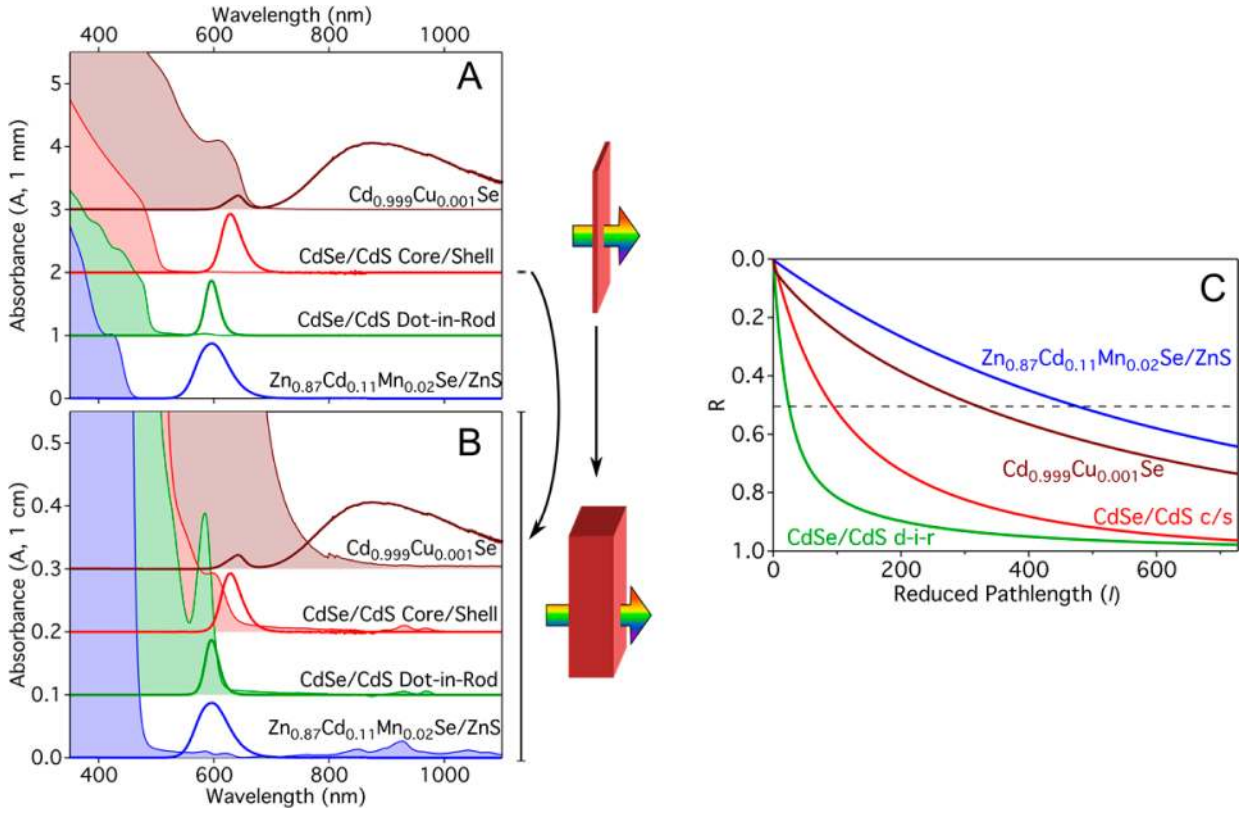

Figure 2. (A) Absorption spectra (solid lines with shading) over a 1 mm path length and dilute photoluminescence spectra of $Cd_{0.999}Cu_{0.001}Se$ (maroon, d = 5.7 nm), CdSe/CdS core/shell NCs (red, core d = 2.7 nm), CdSe/CdS dot-in-rod NCs (green, core d = 2.7 nm), and $Zn_{0.87}Cd_{0.11}Mn_{0.02}Se/ZnS$ (blue, core d = 3.2 nm). (B) Absorption spectra of the same samples measured in a 1 cm path length cuvette illustrating the overlap between absorption and PL. Note the 10× magnified y-axis. (C) Reabsorption probability, $R(l)$, calculated from the spectra in panel B according to eq 1 and plotted versus l. The dashed line indicates $R_{0.5}$, which for a given sample represents the value of l corresponding to 50% probability of reabsorption.

Table 1. Characterization Metrics for Nanocrystalline LSC Phosphors

NC Sample	λ_{thresh} (nm)	$R_{0.5}$[a]	$L_{1/2}$ (cm)[b]	η_{PL}[c]	abs. solar flux[f] ($A_{sol,NC}$) × 10^{20}	projected FG 120 cm × 120 cm 2-D LSC (G = 300)	projected FG_{max} for 2-D LSC
$Zn_{0.87}Cd_{0.11}Mn_{0.02}Se/ZnS$	429	470	118	0.88[d]	1.5	8.6	32.9
$Cd_{0.999}Cu_{0.001}Se$	624	320	42	0.27[d] (0.40[d])	8.9	10.1 (16.0)[g]	15.6 (26.2)[g]
CdSe/CdS core/shell	480	92	12	0.68[d] (0.86[e])	3.3	5.7 (9.0)[g]	7.2 (12.3)[g]
CdSe/CdS dot-in-rod	476	24	4	0.86[d]	2.9	4.2	5.4

[a]Calculated using eq 1. [b]For comparison, measurements with the benchmark organic dye perylene yield $L_{1/2}$ = 4 cm (Supporting Information, Figure S2). [c]Where different from those measured for the samples in Figure 2, the best-reported luminescence quantum yields are given in parentheses. [d]From this work, measured using 385 nm excitation. [e]From ref 19. [f]In units of photons/(m^2 s). For reference, the total solar flux absorbed by bulk Si is 24.8 × 10^{20} photons/(m^2 s) and for bulk CdSe is 11.6 × 10^{20} photons/(m^2 s). [g]Calculated using the best-reported luminescence quantum yield.

important to recognize, however, that the critical transport direction in LSCs is lateral, not normal to the surface, and that lateral device dimensions are typically orders of magnitude larger than the pathlengths used to collect these and other published NC absorption spectra. To illustrate, Figure 2B plots absorption spectra of the same NC solutions measured using a 1 cm path length cuvette and magnified 10-fold for an effective 100× magnification. Absorption features from the CdSe cores of the CdSe/CdS heterostructures are now clearly visible, but the $Zn_{0.87}Cd_{0.11}Mn_{0.02}Se/ZnS$ and $Cd_{0.999}Cu_{0.001}Se$ NCs still show only weak, broad absorption in the vicinity of their PL. On the basis of Mn^{2+}-doped ZnS thin films,[24] the extinction coefficient associated with the luminescent $^6A_1 \rightarrow {}^4T_1$ transition is on the order of 1 $M^{-1}cm^{-1}$, corresponding to an OD of less than 7 × 10^{-5} in Figure 2B. We thus attribute the small tail in the $Zn_{0.87}Cd_{0.11}Mn_{0.02}Se/ZnS$ absorption spectrum to NC surface states, or possibly trace impurities in solution, but not to the luminescent center itself. Indeed, some of this absorption tail could be removed by addition of tributyl phosphine (TBP, see Supporting Information Figure S1), which suggests it may arise from NC surface oxidation. Overall, this feature has an absorbance of 0.01 at 600 nm over 1 cm, and the TBP also contributes small vibrational overtone absorption peaks at 850 and 925 nm. The $Cd_{0.999}Cu_{0.001}Se$ NCs have a small amount of strongly reabsorbed excitonic PL from a subset of undoped NCs, which accounts for roughly 3% of the overall PL. The magnified absorption spectrum of these NCs shows a broad absorption tail that overlaps the blue edge of the red-shifted PL feature (700−850 nm). We attribute this absorption to the $ML_{CB}CT$ transition that is responsible for the PL.[25] Much of

DOI: 10.1021/nl504510t
Nano Lett. 2015, 15, 1315−1323

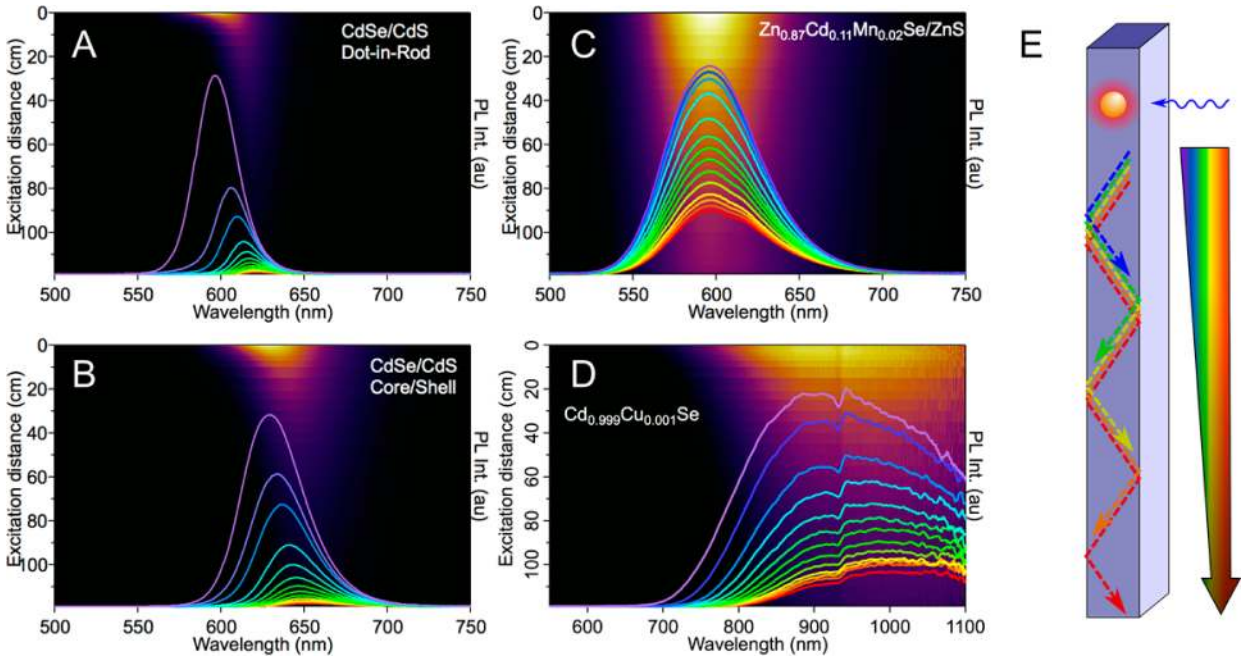

Figure 3. Graphical depictions of PL intensity measured as a function of excitation distance (L) and wavelength for (A) CdSe/CdS dot-in-rod NCs, (B) CdSe/CdS core/shell NCs, (C) $Zn_{0.87}Cd_{0.11}Mn_{0.02}Se/ZnS$ NCs, and (D) $Cd_{0.999}Cu_{0.001}Se$ NCs. Color scales are linear and normalized at L = 0.5 cm. Spectra are overlaid on these images to more precisely illustrate the spectral changes as excitation distance increases from 0.5 cm (purple) to 120 cm (red). (E) Schematic demonstration of distance-dependent attenuation where reabsorption losses preferentially attenuate the blue edge of the spectrum.

the $Cd_{0.999}Cu_{0.001}Se$ PL is shifted to even longer wavelengths (>850 nm), where the absorption spectrum shows only a very small tail that is again likely due to NC surface states.

To assess LSC applicability, the absorption and PL spectra in Figure 2 can be used to estimate the probability of reabsorption of emitted photons by these NCs. One way to do so is to quantify the parameter S introduced in ref 10, which represents the ratio of extinction coefficients at the absorption and emission maxima. S does not take into account the absorption or PL lineshapes, however, and it is difficult to interpret for some NCs that lack a well-defined absorption maximum. Instead, we analyze the probability that an emitted photon will be reabsorbed over a reduced path length l, as given by eq 1[1,26]

$$R(l) = \int PL_{\mathrm{norm}}(\lambda)(1 - 10^{-A_{\mathrm{norm}}(\lambda)\cdot l})\mathrm{d}\lambda \tag{1a}$$

$$l = \frac{L\cdot \mathrm{OD_t}}{t} \tag{1b}$$

Here, $PL_{\mathrm{norm}}(\lambda)$ and $A_{\mathrm{norm}}(\lambda)$ represent the luminescence and absorption spectra, normalized by area and at $\lambda_{\mathrm{thresh}}$, respectively. The reduced path length l is defined in eq 1b and accounts for device geometry trade-offs between luminophore concentration and waveguide thickness (t) governed by Beer's law. For example, the device structure from ref 18 (t = 5 mm, $\mathrm{OD_t}$ = 0.2, L = 21.5 cm) has a maximum l of ~8.6, which corresponds to L = 1.4 cm in the liquid waveguide of Figure 1C (t = 1.65 mm, $\mathrm{OD_t}$ = 1). Other recent NC LSC devices have had maximum l values of ~5.5,[19] ~0.6,[15] and ~53,[17] although exact determination of these values is difficult due to the varying shapes and configurations of these devices. Using eq 1a, $R(l)$ was calculated from each set of spectra in Figure 2 for values of l up to 730 (Figure 2C). $R(l)$ increases most rapidly with increasing l for the two NC heterostructures and less rapidly for the two doped NCs, illustrating smaller reabsorption losses in the latter. Because $R(l)$ is a complex function of l, it cannot be summarized using any single parameter, but we find that the reduced path length at which there is a 50% probability of reabsorption ($R_{0.5}$) provides a useful device-independent luminophore figure of merit calculable from only absorption and PL spectra. Values of $R_{0.5}$ for the nanocrystals of Figure 2 are compiled in Table 1. As anticipated from the spectra of Figure 2B, $R_{0.5}$ is significantly larger for the doped NCs than for the heterostructure NCs, which suggests that LSCs made from the doped NCs should suffer less from reabsorption losses. Although $R(l)$ and $R_{0.5}$ provide useful metrics for estimating reabsorption probabilities, any quantitative prediction of LSC device performance must take into account numerous other factors including device geometry, PL quantum yields, solar absorption, waveguide modes and losses, and scattering losses. It is thus challenging to compare phosphors for large-scale LSC applications with confidence without further experimental input. Motivated by this challenge, we therefore performed a direct empirical comparison of these NCs in the large-scale LSC configuration depicted in Figure 1C.

Solutions of the four NC phosphors described above with $\mathrm{OD_t}$ = 1 (over 1 mm) were loaded into the liquid-waveguide device of Figure 1C. Figure 3A–D show their luminescence spectra collected at different values of L, where L is the distance between the excitation source and the end of the waveguide (see Experimental Methods). The three-dimensional plots show PL intensity as a function of wavelength and L. Figure 3A shows that much of the CdSe/CdS dot-in-rod NC PL is lost within the first few centimeters, and only some of the lowest-energy PL is detectable beyond ~20 cm. The observed PL redshift is due to greater reabsorption losses on the higher energy side of the PL spectrum, as anticipated from Figure 2B and illustrated schematically in Figure 3E. The CdSe/CdS

DOI: 10.1021/nl504510t
Nano Lett. 2015, 15, 1315–1323

core/shell NC data in Figure 3B also show a rapid loss of PL intensity accompanied by a PL red shift with increasing L. In contrast with the NC heterostructures, the two doped NCs show little or no PL redshift with increasing L. Figure 3C plots PL spectra of the $Zn_{0.87}Cd_{0.11}Mn_{0.02}Se/ZnS$ NCs, which decrease gradually in intensity with increasing L, accompanied by only minor spectral changes. These data are consistent with the absorption spectrum in Figure 2B, which shows nearly uniform, weak absorption across the PL energy range. At $L >$ ~50 cm, small dips become evident in the Mn^{2+} PL spectra arising from absorption by C−H stretching harmonics of the surface ligands and solvent. Similar data are obtained for the $Cd_{0.999}Cu_{0.001}Se$ NCs (Figure 3D). As expected from Figure 2, the excitonic emission and the blue edge of the $Cd_{0.999}Cu_{0.001}Se$ $ML_{CB}CT$ PL band are lost to reabsorption, but the red edge decreases only gradually with increasing L. The feature at ~930 nm arises from fiber transmission-loss effects.

Figure 4A summarizes the results of Figure 3 by plotting integrated PL intensities versus L for all four NC phosphors, normalized at $L = 0$. These traces were corrected for waveguide losses, obtained by measuring similar data from 100-fold diluted samples of $Zn_{0.87}Cd_{0.11}Mn_{0.02}Se/ZnS$ and $Cd_{0.999}Cu_{0.001}Se$ NCs, but the uncorrected data are qualitatively very similar (see Supporting Information), confirming that the actual device performance is primarily determined by the phosphor performance. Importantly, because these data were all collected under identical conditions, they allow a quantitative model-independent comparison of these four NCs for potential large-scale LSC applications. The dot-in-rod and core/shell NCs show distinctly nonexponential PL decay with L, whereas the PL from the two doped NCs appears to drop more exponentially with L. The nonexponential decay with L stems from the existence of nonuniform absorption across the PL spectrum in the two heterostructure NCs. This curvature is predicted remarkably well by eq 1, as shown in Figure 2C, confirming this interpretation and the validity of $R(l)$ as a metric for assessing luminophore reabsorption losses in actual waveguides. For comparison with $R_{0.5}$, we parametrize the LSC half-length ($L_{1/2}$),[27] that is, the value of L at which the integrated PL intensity is 50% of its original value. Table 1 summarizes these results and shows that the doped NCs have $L_{1/2}$ values nearly an order of magnitude larger than the NC heterostructures (Table 1). The trend in $L_{1/2}$ values is very similar to that in $R_{0.5}$ with quantitative discrepancies likely due to a combination of photon recycling (not accounted for in $R_{0.5}$) and experimental uncertainties in the absorption spectra. Overall, these measurements emphasize that even small PL reabsorption probabilities can severely impair LSC performance on practical length scales and highlight the critical need for improved luminophores with truly small reabsorption as in the doped NCs described here.

An important outcome of these measurements is the experimental validation of eq 1 as a powerful tool for screening potential LSC luminophores. The relatively simple calculation of $R(l)$ allows evaluation of reabsorption probabilities for any luminophore without the need for device fabrication, and it yields easily interpretable results. Standardization of the assessment of candidate LSC luminophores without preparing and measuring LSCs avoids convolution of luminophore and device performance. In this way, device and luminophore innovations may advance independently from one another.

These experimental data can now be used to predict the solar LSC performance of these same NCs, for example, when the one-dimensional liquid waveguide device of Figure 1C is connected to Si photovoltaics at the waveguide ends and illuminated with the full solar spectrum. Although this linear LSC configuration would not be attractive for most practical applications, the results illustrate the LSC performance of the NCs well. Figure 4B plots projected flux gain (FG) values for the one-dimensional waveguide coupled to Si photovoltaics as a function of LSC length for the same four NCs, calculated according to eq 2[17]

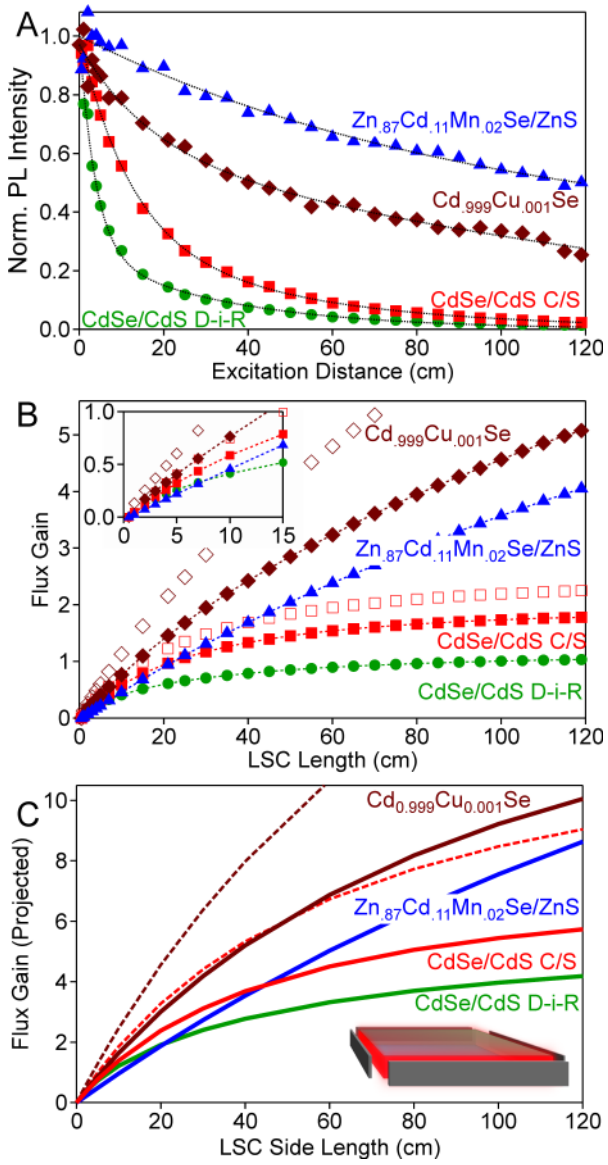

Figure 4. (A) Spectrally integrated PL intensity plotted as a function of excitation distance (L) for CdSe/CdS dot-in-rod NCs (green circles), CdSe/CdS core/shell NCs (red squares), $Cd_{0.999}Cu_{0.001}Se$ NCs (maroon diamonds), and $Zn_{0.87}Cd_{0.11}Mn_{0.02}Se/ZnS$ NCs (blue triangles). Intensities are corrected for waveguide losses. (B) Flux gains of the same four NC samples calculated by eq 2 for the characterization device coupled to Si photovoltaics under AM1.5 solar irradiation plotted as a function of LSC length. Solid symbols use as-measured η_{PL} and open symbols were calculated using best-reported η_{PL} (Table 1). (C) Flux gains calculated for 2D LSC devices coupled to Si photovoltaics under AM1.5 solar irradiation using the same four NC samples, plotted as a function of LSC side length. Solid lines use as-measured η_{PL} and dashed lines used best-reported η_{PL} (Table 1).

DOI: 10.1021/nl504510t
Nano Lett. 2015, 15, 1315−1323

$$\mathrm{FG} = G_{\mathrm{geo}}\eta_{\mathrm{EC}}\cdot\frac{\eta_{\mathrm{PV}}^{\mathrm{PL}}}{\eta_{\mathrm{PV}}^{\mathrm{AM1.5}}}\eta_{\mathrm{PL}}\frac{A_{\mathrm{Sol,NC}}}{A_{\mathrm{Sol,PV}}}\int_0^L I_{\mathrm{PL}}(L)\mathrm{d}L \quad (2)$$

Here, $A_{\mathrm{Sol,NC}}$ and $A_{\mathrm{Sol,PV}}$ are the solar fluxes absorbed by the NCs and the Si PV, respectively, G_{geo} is the geometric gain of the device, η_{PL} is the NC PL quantum yield, η_{EC} is the escape cone loss factor, η_{PV} is the efficiency of the Si PV either at the PL wavelength or under AM 1.5 irradiation as indicated, and $I_{\mathrm{PL}}(L)$ is the experimental distance-dependent waveguided PL intensity reported in Figure 4A. The absorbed solar flux (A_{sol}) is calculated using eq 3, where $A(\lambda)$ represents the absorption spectrum of the PV or LSC, and $S(\lambda)$ represents the solar spectrum in units of photons/(nm m^2 s).

$$A_{\mathrm{Sol}} = \int S(\lambda)(1 - 10^{-A(\lambda)})\mathrm{d}\lambda \quad (3)$$

In the case of the square quartz liquid waveguide used here (Figure 1C), $\eta_{\mathrm{EC}} \sim 0.5$ because there are two escape cones (vertical and horizontal), whereas a planar LSC would have $\eta_{\mathrm{EC}} \sim 0.75$. The ratio $\eta_{\mathrm{PV}}^{\mathrm{PL}}/\eta_{\mathrm{PV}}^{\mathrm{AM1.5}}$ was taken as 1 based on the Panasonic 25.6% efficiency crystalline Si solar cell reported in ref 28, which shows ~100% EQE from 500 to 1000 nm. These calculations were performed using two sets of η_{PL} values, those measured experimentally for the samples of Figure 4A, and the largest reported values (see Table 1). Additionally, to highlight the effects of reabsorption, the FG values presented in Figure 4B were calculated using the PL intensities corrected for waveguide losses, but FGs calculated from raw PL intensities are very similar (Supporting Information, Figure S3), again confirming that the actual device performance is primarily determined by the phosphor performance. Importantly, the FG analysis using eq 2 is validated by experimental measurement of the solar FG for the $Zn_{0.87}Cd_{0.11}Mn_{0.02}Se/ZnS$ NCs using the full-length device of Figure 1C, which yielded a value of FG = 3.7 that is in reasonable agreement with the value predicted for this sample in Figure 4B (FG = 4.1).

For short LSCs (magnified in the inset of Figure 4B), reabsorption losses are not yet dominant and all four NCs show nearly linear increases in FG with L. The slope in this region is determined by the product $A_{\mathrm{Sol,NC}} \times \eta_{\mathrm{PL}}$. Even though the highest observed η_{PL} of $Cd_{1-x}Cu_xSe$ NCs is only 0.4, $A_{\mathrm{Sol,NC}}$ for these NCs is over twice that of the other NCs (Figure 2A, Table 1). The $Cd_{0.999}Cu_{0.001}Se$ NCs are thus the top performer in short LSCs, followed by the CdSe/CdS core/shell NCs. The $Cd_{0.999}Cu_{0.001}Se$ NCs continue to excel as the LSC length increases because of their combination of large $A_{\mathrm{Sol,NC}}$ and small reabsorption losses and thus remain the clear top performer at all 1D LSC lengths examined here. $Cd_{0.999}Cu_{0.001}Se$ NCs therefore outperform all other nanocrystal LSC phosphors reported to date by a significant margin. We note that the highest value of η_{PL} = 0.4 measured here is the highest yet reported for $Cd_{1-x}Cu_xSe$ NCs, but passivation of surface states (e.g., via shell growth) may allow this value to be increased further, as reported for other copper-doped NCs.[29] We have also noticed variations in $L_{1/2}$ due to differences in the nonspecific absorption attributed to surface traps or impurities discussed above (see Supporting Information), for example, we measured $L_{1/2}$ = 51 cm for a different $Cd_{0.999}Cu_{0.001}Se$ NC sample.

It is instructive to compare the CdSe/CdS heterostructures and $Zn_{0.87}Cd_{0.11}Mn_{0.02}Se/ZnS$ NCs in Figure 4B. $A_{\mathrm{Sol,NC}}$ is almost twice as large for both of the heterostructure NCs as for the $Zn_{0.87}Cd_{0.11}Mn_{0.02}Se/ZnS$ NCs, and all have comparable η_{PL}, so the heterostructures perform much better in small LSCs (Figure 4B, inset). As the LSC length increases, however, the heterostructure NCs suffer from major reabsorption losses and their FGs plateau. In contrast, the $Zn_{0.87}Cd_{0.11}Mn_{0.02}Se/ZnS$ NCs show only minor losses with increasing LSC length. They surpass the dot-in-rod NCs at $L \sim 7$ cm, and surpass the core/shell NCs at $L \sim 37$ cm. The lack of a FG plateau up to L = 120 cm with both of the doped NCs highlights the substantially smaller reabsorption in these NCs than in the heterostructure NCs. For large-scale LSC applications, the $Zn_{0.87}Cd_{0.11}Mn_{0.02}Se/ZnS$ NCs are thus superior to the heterostructure NCs despite absorbing less of the solar spectrum. LSCs made with luminophores that do not absorb very much visible light, such as $Zn_{0.87}Cd_{0.11}Mn_{0.02}Se/ZnS$ or related Mn^{2+}-doped NCs, are particularly attractive when transparency is desired, for example, in smart-window applications.

We have additionally extrapolated the performance of these NCs to large-area 2D LSCs. FG was calculated as a function of side length for square LSC devices with t = 1 mm, OD_t = 1, and Si PVs attached to all four edges using the NC absorption and luminescence spectra from Figure 2B along with the η_{PL} values reported in Table 1 (see Supporting Information). Figure 4C plots the calculated FG values versus 2D LSC side length. The trends with increasing LSC size are similar to those found for the 1D device (Figure 4B). In particular, the $Cd_{0.999}Cu_{0.001}Se$ NCs are again the top performer in both small- and reasonably large-area LSCs, despite their relatively low η_{PL}. As anticipated from the 1D measurements and calculations, the $Zn_{0.87}Cd_{0.11}Mn_{0.02}Se/ZnS$ NCs excel at extremely large dimensions, surpassing first the CdSe/CdS core/shell NCs (at an LSC size of ~1.3 m × 1.3 m) and then even the $Cd_{0.999}Cu_{0.001}Se$ NCs (at ~10 m × 10 m, see Supporting Information). Table 1 summarizes the calculated FG values for a device area of 1.2 m × 1.2 m (the square equivalent of our laboratory 1D liquid waveguide), as well as the projected maximum FG values. Overall, these calculations reaffirm the "best-in-class" performance of the new LSC phosphor, $Cd_{0.999}Cu_{0.001}Se$ NCs, on many length scales and validate the use of the 1D waveguide for experimentally assessing the performance of luminophores in large-scale 2D LSCs. The similarity of the size-dependent FG curves for the $Cd_{0.999}Cu_{0.001}Se$ and CdSe/CdS core/shell NCs demonstrates that high PL quantum yields not only improve FG in small LSCs but also mitigate reabsorption losses in large LSCs through increased photon recycling. This principle is also evident from comparison of the curves calculated for the same sample using as-measured and best-reported η_{PL} values (Figure 4).

In summary, semiconductor NCs have recently been proposed as attractive spectral conversion phosphors for next-generation LSCs, but to date a quantitative assessment of these materials for this purpose has been lacking. In this study, we have performed a variety of spectroscopic and one-dimensional waveguide measurements aimed at comparing the leading NC candidates for potential large-scale LSC applications. The experimental results demonstrate that even seemingly small absorption features in the region of luminescence are detrimental to LSC performance on large length scales. CdSe/CdS heterostructure NCs perform well on small length scales but on large length scales they suffer from major losses due to reabsorption of emitted photons. For the two doped NCs, whose luminescent transitions are subject to very little

DOI: 10.1021/nl504510t
Nano Lett. 2015, 15, 1315−1323

reabsorption, the performance at large length scales is in fact limited only by parasitic absorption from vibrational harmonics of the matrix, matrix impurities, surfactants, or NC surface states. These limitations are not intrinsic to the phosphor and can be circumvented. Among the four types of NCs examined here, the "best-in-class" phosphors for full-spectrum concentration by a substantial margin are the $Cd_{1-x}Cu_xSe$ NCs, which absorb the greatest fraction of the solar spectrum and display relatively small reabsorption losses. LSC applications of copper-doped NCs have not been demonstrated previously. The $Zn_{0.87}Cd_{0.11}Mn_{0.02}Se/ZnS$ NCs excel at very large dimensions while retaining visible transparency and are thus attractive for smart-window applications.

In addition to experimental measurements of luminescence in large-scale waveguides, this study presents, and validates with experimental data, a standardized methodology that allows facile prediction of the performance of new luminophores in LSCs from their absorption and PL spectra. The calculation of $R(l)$ using eq 1 allows evaluation of reabsorption for any luminophore without the need for elaborate device fabrication, and it yields easily interpretable results. The predicted reabsorption losses with LSC length agree with experimental results remarkably well, lending credence to flux gains projected from these same experimental parameters for large-scale 2D LSCs. Because the properties of high-performance LSC luminophores are largely independent of any specific LSC device configuration, such independent performance quantification is useful for assessing luminophore potential in a broad suite of LSC technologies.

Finally, we consider the potential for future improvement of NCs as LSC luminophores. The PL quantum yields and solar absorption of the CdSe/CdS heterostructure NCs are both near their theoretical limits, meaning that any improvements must come from reduced reabsorption. Although larger shell volumes would reduce reabsorption, previous studies have pointed out that larger shell thicknesses may lead to reduced[30] or excitation-wavelength dependent[31] quantum yields. Calculations also indicate that Rayleigh scattering from core/shell NCs becomes appreciable over meter-scale pathlengths for NCs with diameters > ~10 nm and that the optimum balance between reabsorption and scattering still involves appreciable losses (see Supporting Information). New heterostructures such as PbSe/CdSe NCs could increase $A_{sol,NC}$ and offset some of the major reabsorption and scattering losses in large-scale LSCs. For the doped NCs, tuning the bandgap (either by size or alloying) and increasing PL quantum yield could potentially increase performance by over a factor of 2. In $Zn_{1-x-y}Cd_xMn_ySe/ZnS$ NCs, tuning λ_{thresh} to ~480 nm by changing size or alloy composition would more than double $A_{sol,NC}$ relative to the NCs reported here without introducing new reabsorption losses. Narrower energy gaps (λ_{thresh} > 480 nm) lead to recovery of excitonic emission via thermal repopulation[32] and would not be beneficial. Similarly, adjusting the energy gap of $Cd_{1-x}Cu_xSe$ NCs to the bulk limit would increase $A_{sol,NC}$ by over 35% relative to the NCs studied here. Even though the best $Cd_{1-x}Cu_xSe$ PL quantum yield achieved here (η_{PL} = 0.4) is the highest yet reported for $Cd_{1-x}Cu_xSe$ NCs, it may be possible to further increase η_{PL} by passivation of surface states, as reported for other copper-doped NCs,[29] which could improve performance of this "best-in-class" phosphor by more than a factor of 2 at all LSC length scales and even more for large-path length devices due to greater photon recycling efficiency (see Supporting Information). Switching from CdSe to other related copper-doped phosphors such as Cu^+:InP[33] or $CuInS_2/ZnS$[29] would yield similarly small PL reabsorption while eliminating Cd^{2+}. A challenge with all of the copper-doped NCs is their broad PL, which begins to extend past the absorption threshold of silicon when the energy gap becomes too narrow. And lastly, the observation that weak, nonspecific absorption attributed to direct excitation of surface traps can be moderated chemically points to the possibility of further improvements in this direction for all NC phosphors. Overall, even with their relatively low η_{PL}, the $Cd_{1-x}Cu_xSe$ NCs reported here combine effective solar absorption with very low reabsorption to substantially outperform all other NCs tested here at all but the largest LSC lengths and areas, marking a significant advance in the development of nanocrystalline phosphors for LSC applications. More generally, these results highlight the attractiveness of doped nanocrystals as phosphors for LSCs.

Experimental Methods. *Synthesis.* All chemicals were used as supplied from Aldrich with the exception of tri-*n*-octyl phosphine (TOP), which was purchased from Strem.

$Zn_{0.87}Cd_{0.11}Mn_{0.02}Se$ NCs. $Zn_{1-x-y}Cd_xMn_ySe$ NCs were grown with slight modifications to previously reported synthetic methods[23] based on the thermal decomposition of the cluster $(NMe_4)_2[Zn_4(SePh)_{10}]$. A flask containing 10.8 g of hexadecyl amine with 12 mg of $MnCl_2{\cdot}4H_2O$ and 15 mg of $CdCl_2$ was first degassed under vacuum at 130 °C for 1 h after which 400 mg of $(NMe_4)_2[Zn_4(SePh)_{10}]$ and 20 mg of Se were added anaerobically. The resulting mixture was again degassed at 130 °C for 1 h before ramping the temperature to 270 °C, where it was held for 15 min before cooling slowly to 100 °C. The resulting NCs were twice crashed out with ethanol, separated by centrifuging, and resuspended in toluene.

$Zn_{0.87}Cd_{0.11}Mn_{0.02}Se/ZnS$ NCs. ZnS shells were grown by transferring the toluene suspension of $Zn_{0.87}Cd_{0.11}Mn_{0.02}Se$ NCs to a flask containing 3g of oleylamine and 3g of octadecane from which the toluene was removed and the resulting suspension degassed for 1 h at 130 °C. $Zn(Oleate)_2$ was prepared by reacting 440 mg of $Zn(OAc)_2$ with 4.4 g of oleic acid and 4.4 mL of octadecene under vacuum at 110 °C until all volatile components were removed. The flask was then put under a nitrogen atmosphere, 36 mg of S dissolved in 3.6 mL of TOP was injected, and the resulting mixture cooled to room temperature. The temperature of the flask containing the NCs was raised to 225 °C and the $Zn(Oleate)_2$-TOP-S mixture was injected via syringe pump at a rate of 0.5 mL/h. The resulting NCs were again purified by flocculation with ethanol followed by resuspension in toluene.

CdSe (Core) NCs. CdSe cores were synthesized according to the standard hot-injection synthesis as reported in ref 16 wherein 60 mg of selenium dissolved in 360 mg of TOP is rapidly injected into a degassed solution of 60 mg of CdO, 280 mg of octadecylphosphonic acid, and 3 g of trioctylphosphine oxide (TOPO) at 380 °C. The heating mantle was removed immediately after injection and the cooled solution of nanocrystals was purified by flocculation with ethanol followed by resuspension in toluene. These NCs had d = 2.7 nm.

CdSe/CdS Core/Shell NCs. CdS shells were grown on the above cores according to ref 19, wherein 20 mL of a 0.08 M $Cd(oleate)_2$ solution in octadecene (ODE) and 20 mL of 2 mM solution of octanethiol in ODE were separately injected at 2.5 mL/h to a degassed solution containing 100 nmol of CdSe cores in 3 mL of ODE and 3 mL of oleylamine at 310 °C. Two milliliters of oleic acid was injected 2 and 4 h after the

DOI: 10.1021/nl504510t
Nano Lett. 2015, 15, 1315−1323

beginning of the injection. After injection was complete, the solution was allowed to stir at 310 °C for an additional 15 min before cooling and purification by flocculation with ethanol followed by resuspension in toluene.

CdSe/CdS Dot-in-Rod NCs. CdS rods were grown onto the above cores according to ref 16, wherein 2 nmol of the CdSe cores dissolved in 1.5 g of TOP with 120 mg of sulfur was injected rapidly into a degassed solution containing 60 mg of CdO, 80 mg of hexylphosphonic acid, 0.29 g of octadecylphosphonic acid, and 3 g of TOPO at 360 °C. After injection, the solution is stirred for 8 min with the temperature recovering to 360 °C, after which it was cooled and purified by flocculation with ethanol followed by resuspension in toluene.

$Cd_{1-x}Cu_xSe$ NCs. $Cd_{1-x}Cu_xSe$ NCs were synthesized by adapting the "heat-up" method for the synthesis of CdSe NCs first reported by Chen et al.[34] Briefly, cadmium myristate (113 mg), selenium dioxide (22 mg), and copper(I) chloride (4 mg) were degassed under vacuum in octadecene (10 g) at room temperature for 30 min. Heating this mixture to 230 °C under nitrogen for 5 min produced a dark brown solution. After dropwise addition of 0.2 mL of oleic acid, the mixture was cooled to room temperature. Addition of 1 volume equivalent of anhydrous ethanol followed by centrifugation produced dark brown pellets that were resuspended in toluene, sonicated, and centrifuged again to remove insoluble impurities. Any adventitious CuSe formed during the reaction was reduced and removed by adding ~0.5 mL of TOP followed by flocculation with ethanol and resuspension in toluene or tetrachloroethylene. Quantum yields as high as 0.4 were measured for these $Cd_{1-x}Cu_xSe$ NCs, but synthetic conditions were not optimized to reproduce this high quantum yield in batches large enough to fill the liquid waveguide. These quantum yields are higher than the previous best reported value for $Cd_{1-x}Cu_xSe$ NCs of 0.25.[35]

Spectroscopy and Characterization. Absorption measurements were taken using a Cary 500 spectrometer, and PL was measured using an Ocean Optics USB-2000+ spectrometer or a liquid-nitrogen-cooled CCD (Acton) coupled to a 0.5m monochromator (for $Cd_{0.999}Cu_{0.001}Se$ measurements), both corrected for spectral sensitivity. Quantum yields were measured using a Hamamatsu integrating sphere quantum yield measurement system with 385 nm excitation. TEM images were collected on an FEI Tecnai microscope, and NC compositions were determined by inductively coupled plasma-atomic emission spectrometry.

The liquid waveguide apparatus for measuring LSC reabsorption losses (Figure 1C) is based on a 120 cm long square quartz tube (supplied by Friederick and Dimmock Co.) with a 1 mm inner dimension (1.65 mm outer dimension) suspended over a black aluminum channel that was illuminated by a 1 mm spot from a 385 nm LED at variable distances from the end. Waveguided light was then collected through high numerical aperture (NA = 0.79) lenses through a diffuser to ensure equivalent collection of all waveguide modes, and measured using a fiber-coupled spectrometer. Because one end of the tube was sealed and flattened to avoid effects of a meniscus on detection, the tube was filled with toluene solutions of luminophore through a removable capillary. Because the $Cd_{0.999}Cu_{0.001}Se$ NC PL overlaps with strong vibrational overtones of toluene (see Supporting Information, Figure S4), these NCs were measured in tetrachloroethylene. Before measurement, each sample was filtered through a 200 nm pore-size PTFE syringe filter. Photographs of this device are provided in Supporting Information, Figure S5.

■ ASSOCIATED CONTENT

Ⓢ Supporting Information

Additional experimental and calculated results (eight figures) and details pertaining to the calculation of 2D LSC flux gains. This material is available free of charge via the Internet at http://pubs.acs.org.

■ AUTHOR INFORMATION

Corresponding Author

*E-mail: gamelin@chem.washington.edu.

Notes

The authors declare no competing financial interest.

■ ACKNOWLEDGMENTS

The authors thank Professor David Patrick, Professor John Gilbertson, Christian Erickson, Alina Schimpf, and Heidi Nelson for valuable assistance. Financial support from the U.S. National Science Foundation (DMR-1206221 to D.R.G. and DMR-1035512 to S.M.) and U.S. Department Of Energy (Office of Energy Efficiency and Renewable Energy (DOE-EERE) Postdoctoral Research Award to K.E.K.) is also gratefully acknowledged. Part of this work was conducted at the University of Washington NanoTech User Facility, a member of the NSF National Nanotechnology Infrastructure Network (NNIN).

■ REFERENCES

(1) Batchelder, J. S.; Zewai, A. H.; Cole, T. Luminescent solar concentrators. 1: Theory of operation and techniques for performance evaluation. *Appl. Opt.* **1979**, *18*, 3090−3110.

(2) Reisfeld, R.; Shamrakov, D.; Jorgensen, C. Photostable solar concentrators based on fluorescent glass films. *Sol. Energy Mater. Sol. Cells* **1994**, *33*, 417−427.

(3) Debije, M. G.; Verbunt, P. P. C. Thirty Years of Luminescent Solar Concentrator Research: Solar Energy for the Built Environment. *Adv. Energy Mater.* **2012**, *2*, 12−35.

(4) McIntosh, K. R.; Yamada, N.; Richards, B. S. Theoretical comparison of cylindrical and square-planar luminescent solar concentrators. *Appl. Phys. B: Laser Opt.* **2007**, *88*, 285−290.

(5) Bornstein, J. G. Luminescent Solar Concentrator Daylighting. *Proc. SPIE* **1984**, DOI: 10.1117/12.944798.

(6) Earp, A. A.; Smith, G. B.; Franklin, J.; Swift, P. Optimisation of a three-colour luminescent solar concentrator daylighting system. *Sol. Energy Mater. Sol. Cells* **2004**, *84*, 411−426.

(7) Fisher, B.; Biddle, J. Luminescent spectral splitting: Efficient spatial division of solar spectrum at low concentration. *Sol. Energy Mater. Sol. Cells* **2011**, *95*, 1741−1755.

(8) Hammam, M.; El-Mansy, M. K.; El-Bashir, S. M.; El-Shaarawy, M. G. Performance evaluation of thin-film solar concentrators for greenhouse applications. *Desalination* **2007**, *209*, 244−250.

(9) de Boer, D. K. G.; Broer, D. J.; Debije, M. G.; Keur, W.; Meijerink, A.; Ronda, C. R.; Verbunt, P. P. C. Progress in phosphors and filters for luminescent solar concentrators. *Opt. Express* **2012**, *20*, A395−A405.

(10) Currie, M. J.; Mapel, J. K.; Heidel, T. D.; Goffri, S.; Baldo, M. A. High-Efficiency Organic Solar Concentrators for Photovoltaics. *Science* **2008**, *321*, 226−228.

(11) Wilson, L. R. Luminescent Solar Concentrators: A Study of Optical Properties, Re-Absorption and Device Optimization. Doctoral Thesis, Heriot-Watt University, Edinburgh, 2010.

(12) Bomm, J.; Büchtemann, A.; Chatten, A. J.; Bose, R.; Farrell, D. J.; Chan, N. L. A.; Xiao, Y.; Slooff, L. H.; Meyer, T.; Meyer, A.; van

DOI: 10.1021/nl504510t
Nano Lett. 2015, 15, 1315−1323

Sark, W. G. J. H. M.; Koole, R. Fabrication and Full Characterization of State-of-the-Art Quantum Dot Luminescent Solar Concentrators. *Sol. Energy Mater. Sol. Cells* **2011**, *95*, 2087−2094.
(13) Inman, R. H.; Shcherbatyuk, G. V.; Medvedko, D.; Gopinathan, A.; Ghosh, S. Cylindrical luminescent solar concentrators with near-infrared quantum dots. *Opt. Express* **2011**, *19*, 24308−24313.
(14) Purcell-Milton, F.; Gun'ko, Y. K. Quantum dots for Luminescent Solar Concentrators. *J. Mater. Chem.* **2012**, *22*, 16687−16697.
(15) Krumer, Z.; Pera, S. J.; van Dijk-Moes, R. J. A.; Zhao, Y.; de Brouwer, A. F. P.; Groeneveld, E.; van Sark, W. G. J. H. M.; Schropp, R. E. I.; de Mello Donega, C. Tackling self-absorption in luminescent solar concentrators with type-II colloidal quantum dots. *Sol. Energy Mater. Sol. Cells* **2013**, *111*, 57−65.
(16) Bronstein, N. D.; Li, L.; Xu, L.; Yao, Y.; Ferry, V. E.; Alivisatos, A. P.; Nuzzo, R. G. Luminescent Solar Concentration with Semiconductor Nanorods and Transfer-Printed Micro-Silicon Solar Cells. *ACS Nano* **2013**, *8*, 44−53.
(17) Erickson, C. S.; Bradshaw, L. R.; McDowall, S.; Gilbertson, J. D.; Gamelin, D. R.; Patrick, D. L. Zero-Reabsorption Doped-Nanocrystal Luminescent Solar Concentrators. *ACS Nano* **2014**, *8*, 3461−3467.
(18) Meinardi, F.; Colombo, A.; Velizhanin, K. A.; Simonutti, R.; Lorenzon, M.; Beverina, L.; Viswanatha, R.; Klimov, V. I.; Brovelli, S. Large-area luminescent solar concentrators based on "Stokes-shift-engineered" nanocrystals in a mass-polymerized PMMA matrix. *Nat. Photonics* **2014**, *8*, 392−399.
(19) Coropceanu, I.; Bawendi, M. G. Core/Shell Quantum Dot Based Luminescent Solar Concentrators with Reduced Reabsorption and Enhanced Efficiency. *Nano Lett.* **2014**, *14*, 4097−4101.
(20) Yoon, J.; Li, L.; Semichaevsky, A. V.; Ryu, J. H.; Johnson, H. T.; Nuzzo, R. G.; Rogers, J. A. Flexible concentrator photovoltaics based on microscale silicon solar cells embedded in luminescent waveguides. *Nat. Commun.* **2011**, *2*, 343.
(21) Shen, Y.; Jia, Y.; Sheng, X.; Shen, L.; Rogers, J. A.; Giebink, N. C. Nonimaging Optical Gain in Luminescent Concentration through Photonic Control of Emission Étendue. *ACS Photonics* **2014**, *1*, 746−753.
(22) Yin, Y.; Alivisatos, A. P. Colloidal nanocrystal synthesis and the organic-inorganic interface. *Nature* **2005**, *437*, 664−670.
(23) McLaurin, E. J.; Fataftah, M. S.; Gamelin, D. R. One-step synthesis of alloyed dual-emitting semiconductor nanocrystals. *Chem. Commun.* **2013**, *49*, 39−41.
(24) McClure, D. S. Optical Spectra of Exchange Coupled Mn++ Ion Pairs in ZnS:MnS. *J. Chem. Phys.* **1963**, *39*, 2850−2855.
(25) Suzuki, A.; Shionoya, S. Mechanism of the Green-Copper Luminescence in ZnS Crystals. I. Direct Evidence for the Pair Emission Mechanism. *J. Phys. Soc. Jpn.* **1971**, *31*, 1455−1461.
(26) Birks, J. B. *Photophysics of Aromatic Molecules*; Wiley-Interscience: London, 1970.
(27) Earp, A. A.; Smith, G. B.; Swift, P. D.; Franklin, J. Maximising the light output of a Luminescent Solar Concentrator. *Sol. Energy* **2004**, *76*, 655−667.
(28) Green, M. A.; Emery, K.; Hishikawa, Y.; Warta, W.; Dunlop, E. D. Solar cell efficiency tables (version 44). *Prog. Photovoltaics* **2014**, *22*, 701−710.
(29) Zhang, W.; Lou, Q.; Ji, W.; Zhao, J.; Zhong, X. Color-Tunable Highly Bright Photoluminescence of Cadmium-Free Cu-Doped Zn-In-S Nanocrystals and Electroluminescence. *Chem. Mater.* **2013**, *26*, 1204−1212.
(30) Ghosh, Y.; Mangum, B. D.; Casson, J. L.; Williams, D. J.; Htoon, H.; Hollingsworth, J. A. New Insights into the Complexities of Shell Growth and the Strong Influence of Particle Volume in Nonblinking "Giant" Core/Shell Nanocrystal Quantum Dots. *J. Am. Chem. Soc.* **2012**, *134*, 9634−9643.
(31) Wu, K.; Rodríguez-Córdoba, W. E.; Liu, Z.; Zhu, H.; Lian, T. Beyond Band Alignment: Hole Localization Driven Formation of Three Spatially Separated Long-Lived Exciton States in CdSe/CdS Nanorods. *ACS Nano* **2013**, *7*, 7173−7185.
(32) Vlaskin, V. A.; Janßen, N.; van Rijssel, J.; Beaulac, R.; Gamelin, D. R. Tunable Dual Emission in Doped Semiconductor Nanocrystals. *Nano Lett.* **2010**, *10*, 3670−3674.
(33) Xie, R.; Peng, X. Synthesis of Cu-Doped InP Nanocrystals (d-dots) with ZnSe Diffusion Barrier as Efficient and Color-Tunable NIR Emitters. *J. Am. Chem. Soc.* **2009**, *131*, 10645−10651.
(34) Chen, O.; Chen, X.; Yang, Y.; Lynch, J.; Wu, H.; Zhuang, J.; Cao, Y. C. Synthesis of Metal−Selenide Nanocrystals Using Selenium Dioxide as the Selenium Precursor. *Angew. Chem. Int. Ed.* **2008**, *47*, 8638−8641.
(35) Grandhi, G. K.; Tomar, R.; Viswanatha, R. Study of Surface and Bulk Electronic Structure of II−VI Semiconductor Nanocrystals Using Cu as a Nanosensor. *ACS Nano* **2012**, *6*, 9751−9763.

DOI: 10.1021/nl504510t
Nano Lett. 2015, 15, 1315−1323

Supplementary Information For:

Nanocrystals for Luminescent Solar Concentrators

Liam R. Bradshaw,[a] Kathryn E. Knowles,[a] Stephen McDowall,[b] Daniel R. Gamelin[a,*]

[a]*Department of Chemistry, University of Washington, Seattle, Washington 98195-1700, United States,* [b]*Mathematics Department, Western Washington University, 516 High Street, Bellingham, Washington 98225, United States*
e-mail: *Gamelin@chem.washington.edu*

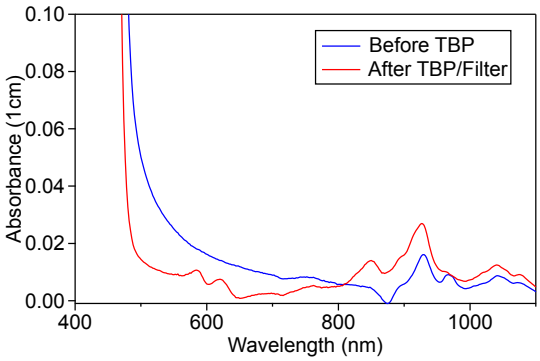

Figure S1. Absorption spectra measured over 1 cm pathlength of $Zn_{0.87}Cd_{0.11}Mn_{0.02}Se/ZnS$ NCs with OD_t = 1 (over 1 mm) as synthesized (blue) and after reduction with tri-butyl phosphine and filtration (red).

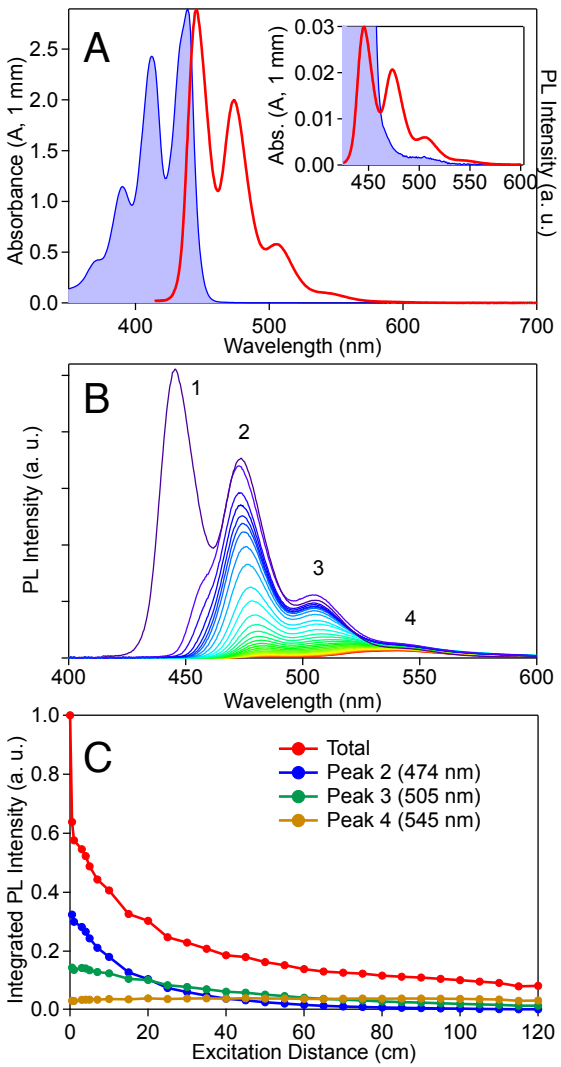

Figure S2. (A) Absorption (blue shaded) and dilute PL (red) spectra of perylene. The absorption spectrum was taken from the solution used for distance-dependent excitation experiments, in a 1 mm cuvette. The inset shows the same spectra, with the absorption spectrum magnified 100x. **(B)** Excitation-distance dependent PL spectra from L = 0 - 120 cm. The L = 0 cm spectrum was calculated by fitting the plot of the intensity of peak "2" versus L to a single exponential, and scaling the dilute PL spectrum to match this fit at L = 0 cm. **(C)** Plot of integrated PL intensity versus L for the total spectrum (red), and the individual peaks following the labeling in panel (B). Note that peak 4 actually increases with increasing L because of photon recycling.

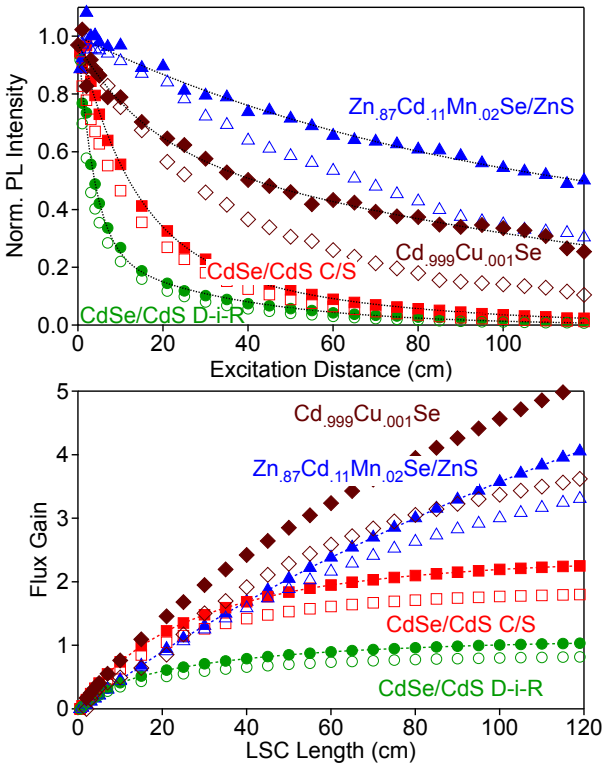

Figure S3. Plots of **(A)** measured PL intensity versus excitation distance *L* and **(B)** calculations of flux gain as a function of LSC length (as in Figure 4 of the main text), shown for raw PL intensities (open symbols) and PL intensities corrected for waveguide losses (closed symbols).

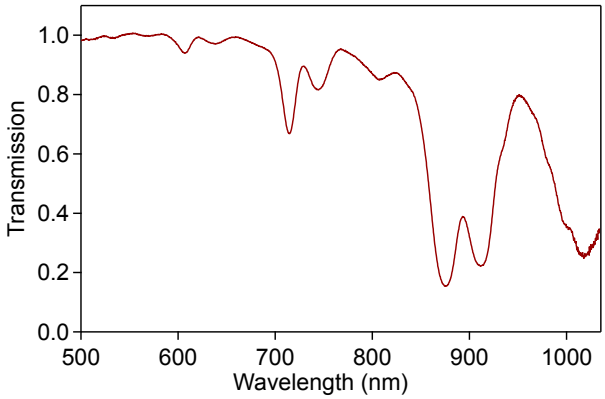

Figure S4. Transmission spectrum of toluene over 120 cm collected by coupling the light from a halogen lamp into the back end of the quartz waveguide from Figure 1C and comparing spectra from the empty and toluene-filled waveguide.

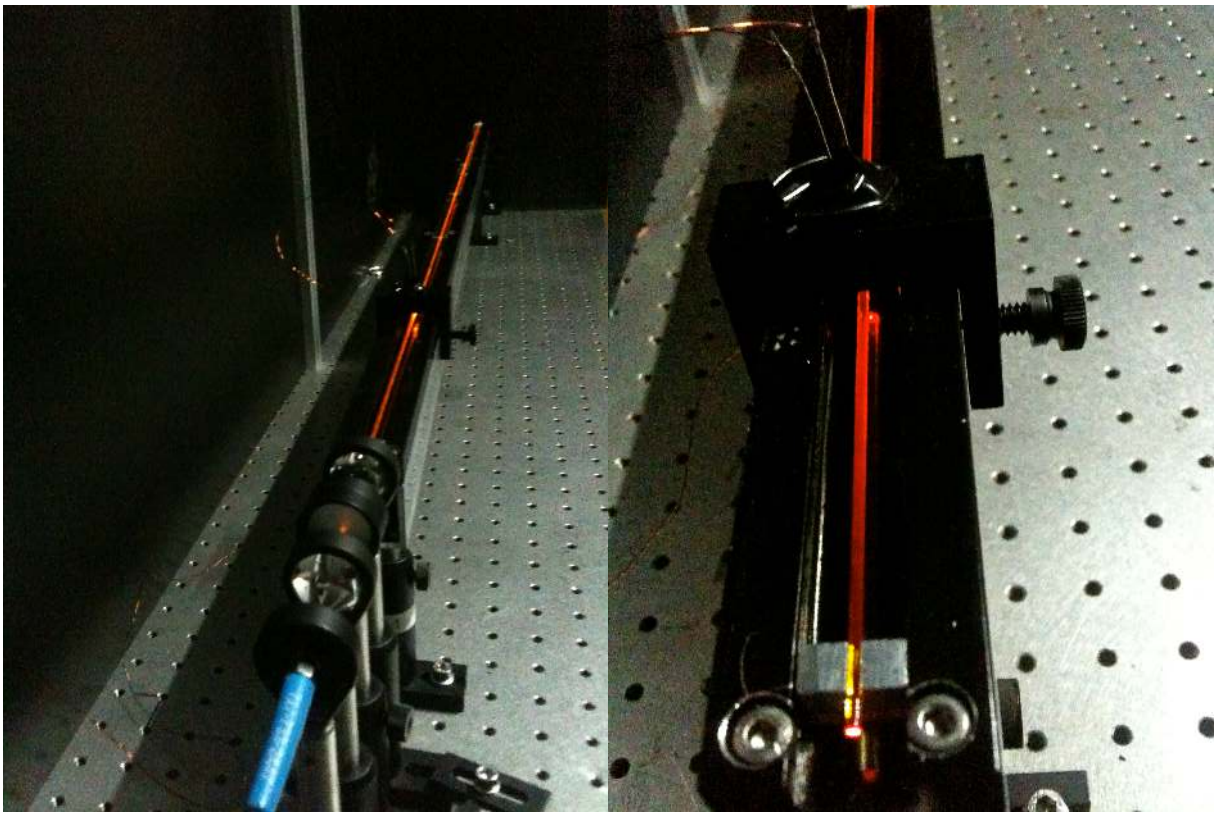

Figure S5. Photographs of the liquid waveguide showing the entire device and collection optics (left), and a close-up of the end of the tube and the movable excitation source (right).

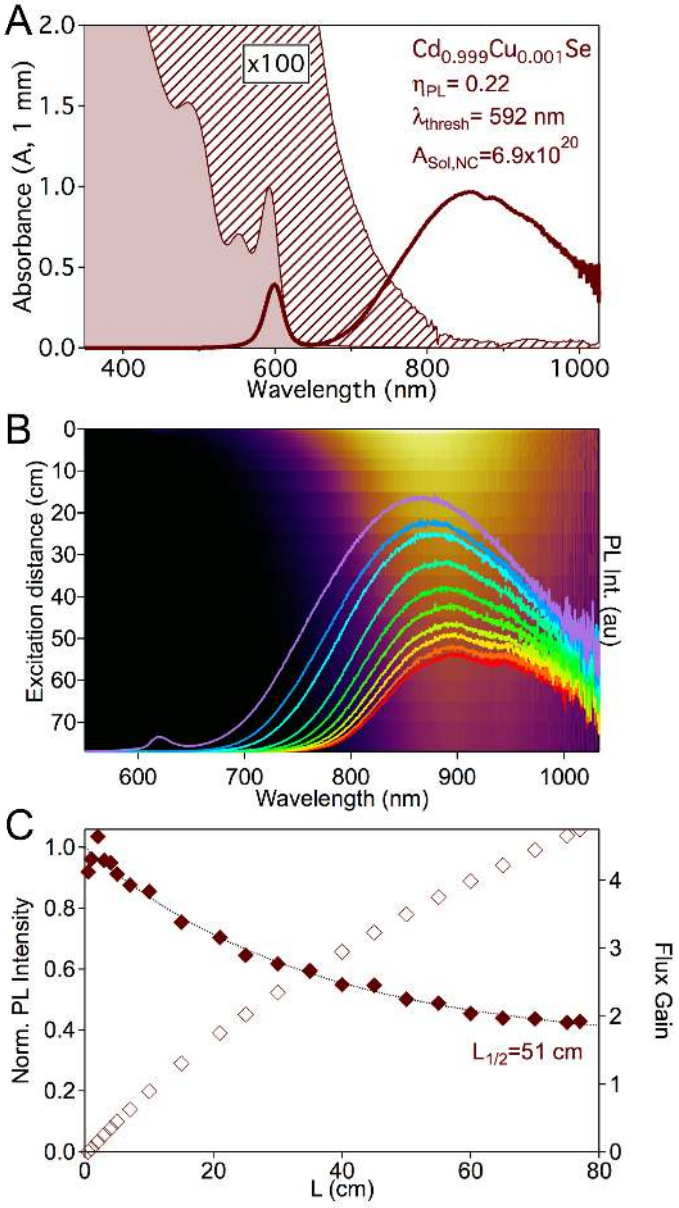

Figure S6. (A) Absorbance (shaded and diagonally patterned) and PL spectra (curve), **(B)** PL excitation distance dependence, and **(C)** L dependence of integrated PL intensity (left axis, closed symbols) and calculated FG (open symbols, right axis) for a different sample of $Cd_{0.999}Cu_{0.001}Se$ NCs than was used in the main text. Solar absorption is stated in units of photons/(m^2 sec). $L_{1/2}$ is significantly greater with these NCs than those in the main text. These NCs were not used in the main text because of the limited sample volume and their smaller solar absorption.

Calculation of 2-D LSC Flux Gain.

In terms of OQE (the proportion of absorbed photons that reach the PV-covered edge of the LSC), the flux gain for a square $L\times L$ LSC is given by equation S1:

$$FG = G_{geo}(L) \cdot \frac{\eta_{PV}^{pl}}{\eta_{PV}^{AM\,1.5}} \cdot OQE(L). \quad [S1]$$

Here, $G_{geo}(L) = L^2/4Lt = L/4t$ where t is the LSC thickness. To compute OQE, under the assumption that there is no scattering, we first compute what proportion of emitted photons reach an edge of the LSC *without* being re-absorbed by a NC. This is governed by $PL(\lambda)$ and $A(\lambda)$ and is given by equation S2:

$$\rho(L) = \frac{1}{4\pi L^2} \iint_{L\times L} \int_0^{2\pi} \int_{\theta_{esc}}^{\pi-\theta_{esc}} \int PL(\lambda) 10^{-A(\lambda)\, l(x,y,\theta,\phi)} \sin\theta \; d\lambda \, d\theta \, d\phi \, dx \, dy \quad [S2]$$

Here, $l(x, y, \theta, \phi)$ is the distance a photon will travel from position (x, y) in the LSC, in direction (θ, ϕ) (in spherical coordinates) before reaching the edge of the LSC; $PL(\lambda)$ is the probability that an emitted photon has wavelength λ, and $10^{-A(\lambda)\, l(x,y,\theta,\phi)}$ is the probability that the photon will travel distance l given it has wavelength λ; θ_{esc} is the angle of the escape-cone.

From knowledge of $\rho(L)$ we compute $OQE(L)$ as follows: we make the assumption that the distribution of absorbed photons is uniform over the area of the LSC, and furthermore, that subsequent absorption events of recycled photons are also uniform over the LSC. From the initial absorption of photons, η_{PL} are emitted, $(1 - \eta_{PL}) + (1 - \eta_{EC})\eta_{PL} = 2 - \eta_{PL} - \eta_{EC}\eta_{PL}$ are lost due to less than unity quantum efficiency and due to escape-cone loss, and the proportion of photons which will reach the edge is $\rho\,\eta_{PL}$. The proportion that remains in the LSC is thus $1 - (2 - \eta_{PL} - \eta_{EC}\eta_{PL}) - \rho\,\eta_{PL} = \eta_{PL}(\eta_{EC} - \rho)$. Under the assumption that these remaining photons are absorbed uniformly over the LSC, second emission photons experience the same mechanism, and so $(2 - \eta_{PL} - \eta_{EC}\eta_{PL})(\eta_{PL}(\eta_{EC} - \rho))$ are lost, and $\rho\,\eta_{PL}(\eta_{PL}(\eta_{EC} - \rho))$ reach the edge of the LSC. What remains in the LSC is given by equation S3:

$$\eta_{PL}(\eta_{EC} - \rho) - (2 - \eta_{PL} - \eta_{EC}\eta_{PL})\big(\eta_{PL}(\eta_{EC} - \rho)\big) - \rho\,\eta_{PL}\big(\eta_{PL}(\eta_{EC} - \rho)\big) = \eta_{PL}^2(\eta_{EC} - \rho)^2 \quad [S3]$$

Repeating this process and summing over all absorption/re-emission events we arrive at the proportion of captured photons expressed in equation S4:

$$OQE(L) = \rho(L)\eta_{PL} \sum_{n=0}^{\infty} [\eta_{PL}(\eta_{EC} - \rho(L))]^n \; = \frac{\rho(L)\eta_{PL}}{1 - \eta_{PL}(\eta_{EC} - \rho(L))} \quad [S4]$$

Flux gain is then calculated by application the result of equation S4 to equation S1 for any side length, *L*. Results calculated for the four nanocrystals of the main manuscript are plotted in Figure S7.

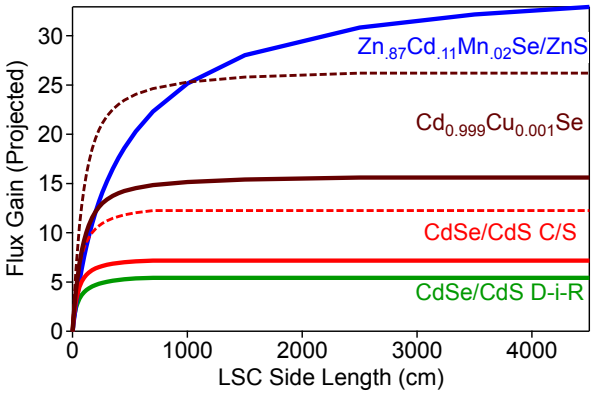

Figure S7. Projected flux gains for 1 mm thick, OD_t = 1 square-planar nanocrystal LSCs coupled to Si photovoltaics, under AM 1.5 solar irradiation, plotted as a function of side length. Dashed lines were calculated using best-reported quantum yields from Table 1.

Scattering by nanocrystals.

Figure S8 shows calculations of the contributions of Rayleigh scattering to losses over a 1 m pathlength in a nanocrystal LSC device. Effective absorbance was calculated according to equation S1,

$$A_R = \frac{2\pi^5}{3}\frac{d^6}{\lambda^4}\left(\frac{n_{dot}^2 - n_{sol}^2}{n_{dot}^2 + 2n_{sol}^2}\right)^2 \frac{C \cdot 100cm}{3.8 \cdot 10^{-17}} P_{EC} \qquad [S5]$$

where d is the diameter of the nanocrystal, n_{dot} is the index of refraction of the semiconductor (~2.5), n_{sol} is the index of refraction of the solvent (~1.5), and P_{EC} is the probability of escape cone loss from a scattering event, approximated as 20% based on the 1 + $\cos^2(\theta)$ angular anisotropy of Rayleigh scattering. The concentration of nanocrystals, C, was chosen to maintain an OD_t = 1 over 1 mm based on literature values for size dependent extinction coefficients.[1, 2] This qualitative model neglects effects of size distributions and changes in the size dependence of the extinction coefficient beyond the range measured in refs. 1 and 2. The wavelength, λ, is taken as the emission maximum for systems similar to those reported herein: ZnSe/ZnS, λ = 600 nm where Mn^{2+} emits; CdS NCs are assumed to emit as CdSe/CdS core shells at 625 nm; CdSe NCs are assumed to emit at 1000 nm either from $Cu^{+/2+}$ charge transfer or from sensitization of a PbSe core (for example).

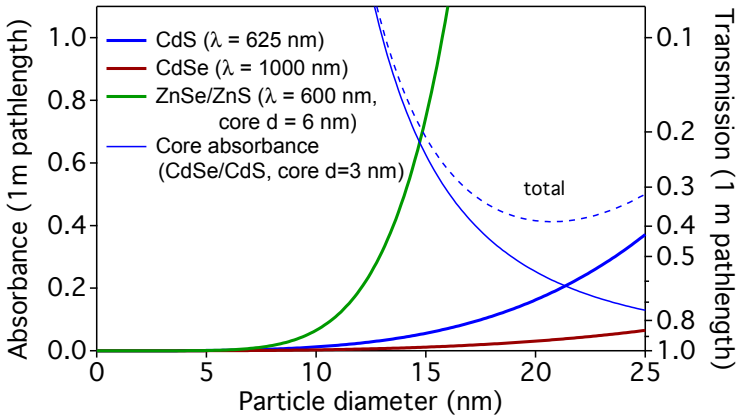

Figure S8. Calculated effective absorbance (left axis) and transmission (right axis) over 1 m due to Rayleigh scattering from CdS (blue), CdSe (red) and ZnSe/ZnS (green) NCs as a function of nanocrystal diameter. Scattering for CdS and CdSe nanocrystals was calculated at 625 nm and 1000 nm, respectively, and their concentration decreases as they get larger to maintain an $OD_t = 1$. Scattering for ZnSe/ZnS nanocrystals was calculated at 600 nm, with a constant concentration based on a core diameter of 6 nm and increasing the total diameter by only changing the shell thickness. The waveguide index of refraction was 1.5, and escape cone losses from a scattering event were taken to be 20%. Also shown is the effective absorbance (assuming unity QY and 25% escape cone loss) from reabsorption by the core for a CdSe/CdS nanocrystal with a 3 nm core (fine blue line), and total losses (dashed blue) for such a nanocrystal.

Also shown in Figure S8 is the calculated reabsorption at 625 nm from the core in a CdSe/CdS core/shell nanocrystal as a function of nanocrystal diameter. Still working at the 625 nm emission maximum, this curve is calibrated using our 13.5 nm nanocrystals, which have a 1 m OD (measured from Figure 2B) of 3.6. Assuming 100% PL quantum yield, a 25% escape cone loss per reabsorption leads to an effective 1 m OD of 0.9. Addition of the scattering and core absorption curves yields the dashed curve in Figure S8, which indicates that particles with $d \sim 20$ nm minimize total losses. Although these calculations may not be quantitatively accurate, they illustrate the existence of an optimal size for core/shell NCs to balance scattering and reabsorption losses, and even at this size these losses are substantial.

References

1. Yu, W. W.; Qu, L.; Guo, W.; Peng, X., Experimental Determination of the Extinction Coefficient of CdTe, CdSe, and CdS Nanocrystals. *Chem. Mater.* 2003, **15** (14), 2854-2860.
2. Norberg, N. S.; Parks, G. L.; Salley, G. M.; Gamelin, D. R., Giant Excitonic Zeeman Splittings in Colloidal Co^{2+}-Doped ZnSe Quantum Dots. *J. Am. Chem. Soc.* 2006, **128** (40), 13195-13203.